Basicity of Isostructural Porous Ionic Crystals Composed of Nb/Ta-Substituted Keggin-Type Polyoxotungstates

Journal:	*Dalton Transactions*
Manuscript ID	DT-ART-02-2022-000478.R2
Article Type:	Paper
Date Submitted by the Author:	21-Apr-2022
Complete List of Authors:	Weng, Zhewei; The University of Tokyo Graduate School of Arts and Sciences College of Arts and Sciences Ogiwara, Naoki; The University of Tokyo Graduate School of Arts and Sciences, ; Yokogawa, Daisuke; The University of Tokyo Kitao, Takashi; The University of Tokyo; The University of Tokyo, Kikukawa, Yuji; Kanazawa University Institute of Science and Engineering, Uchida, Sayaka; The University of Tokyo,

COMMUNICATION

Basicity of Isostructural Porous Ionic Crystals Composed of Nb/Ta-Substituted Keggin-Type Polyoxotungstates

Zhewei Weng,[a] Naoki Ogiwara,[a] Daisuke Yokogawa,[a] Takashi Kitao,[b,c] Yuji Kikukawa,[d] Sayaka Uchida*[a]

Received 00th January 20xx,
Accepted 00th January 20xx

DOI: 10.1039/x0xx00000x

Three isostructural porous ionic crystals (PICs) based on Keggin-type POMs with different compositions but equal negative charge ($[BW_{12}O_{40}]^{5-}$ (BW_{12}), $[SiW_{11}NbO_{40}]^{5-}$ ($SiW_{11}Nb$), and $[SiW_{11}TaO_{40}]^{5-}$ ($SiW_{11}Ta$)) are synthesized. Experimental and theoretical characterizations of the three PICs (1_BW_{12}, 1_$SiW_{11}Nb$, and 1_$SiW_{11}Ta$) show that the substitution of Nb/Ta for W in the POMs enhances the basicity of PICs, which increases in the order of 1_BW_{12} < 1_$SiW_{11}Nb$ < 1_$SiW_{11}Ta$. These findings clearly show that the increase in basicity is due not only to the increase in negative charge of the POM molecule as is often explained, but also to the character of the substituted element itself.

Base-catalyzed reactions, such as the isomerization of alkene/alkynes, C–C bond formation, and hydrogenation, are important for manufacturing bulk and fine chemicals.[1–4] Although acids can catalyze most of the reactions above, there are several advantages in base-catalyzed reactions, such as less byproducts and activation of organic compounds with heteroatoms (N, O).[5–7] A particular focus has been given on solid base catalysts, such as alkali ion-exchanged zeolites and alkaline earth metal oxides, due to their thermal stability and recyclability.[8–10] However, the development of solid base catalysts is well behind solid acid catalysts,[11–14] because it is difficult to construct electrically and structurally controlled uniform basic sites in solids. Therefore, the design and synthesis of solid base catalysts with well-defined active sites remain a strongly desired and challenging research subject.

Polyoxometalates (POMs) are a large family of anionic metal oxide clusters containing early transition metals.[15–18] POMs are considered as promising solid base catalysts because of the following properties. (i) The abundant surface metal-oxo moieties (M=O and M–O–M) act as basic sites promoting nucleophilic abstraction of proton from the reactant molecules. (ii) The molecular structures and compositions of POMs can be fine-tuned to enhance their basicity.[19] In an early work, López *et al.* verified by DFT calculation that a V-trisubstituted POM $[SiW_9V_3O_{40}]^{7-}$ possesses higher basicity than a Mo-trisubstituted POM $[SiW_9Mo_3O_{40}]^{4-}$.[20] Recently, several groups have reported that Nb/Ta-containing POMs show high basicity due to the lower oxidation states of Nb/Ta (+5) compared with Mo/W (+6), leading to the formation of more negatively charged POMs suitable for proton abstraction.[21–25]

In this regard, we recently reported a series of porous ionic crystals (PICs) composed of Nb/Ta-substituted Dawson-type POMs with a molecular cation (macrocation) serving as efficient solid base catalysts.[26] However, the crystal structures varied among the PICs, so that we failed to establish a firm composition–structure–function relationship. Therefore, we reached the idea that isostructural PICs with different compositions would serve as a platform to clarify the effects of composition towards function (base catalysis). Based on these considerations, in this work, we synthesized three isostructural PICs composed of a series of Keggin-type POMs with an equal negative charge (–5) and a macrocation ($[Cr_3O(OOCH)_6(H_2O)_3]^+$, **Cr-H**) (Fig. 1). Specifically, a non-substituted POM ($[BW_{12}O_{40}]^{5-}$: $\mathbf{BW_{12}}$) or Nb/Ta mono-substituted POMs ($[SiW_{11}NbO_{40}]^{5-}$: $\mathbf{SiW_{11}Nb}$ and $[SiW_{11}TaO_{40}]^{5-}$: $\mathbf{SiW_{11}Ta}$) were used as building blocks to clarify the effects of Nb/Ta-substitution on the basicity of PICs.

The PICs (**1_POMs**) crystallized from aqueous nitric acid solutions containing $[Cr_3O(OOCH)_6(H_2O)_3](OOCH)\cdot nH_2O$, potassium salt of the corresponding POM, and KCl.[‡] The FT-IR spectra of the **1_POMs** showed characteristic peaks of the macrocation and POMs (Figs. S1–S3). Elemental analyses were carried out with inductively coupled plasma optical emission

---

[a] Department of Basic Science, School of Arts and Sciences, The University of Tokyo, 3-8-1 Komaba, Meguro-ku, Tokyo 153-8902, Japan.
[b] Department of Applied Chemistry, School of Engineering, The University of Tokyo, 7-3-1 Hongo, Bunkyo-ku, Tokyo 113-8656, Japan.
[c] Department of Advanced Materials Science, Graduate School of Frontier Sciences, The University of Tokyo, 5-1-5 Kashiwanoha, Kashiwa, Chiba 277-8561, Japan.
[d] Department of Chemistry, Graduate School of Natural Science and Technology, Kanazawa University, Kakuma-machi, Kanazawa, Ishikawa 920-1192, Japan.

Electronic Supplementary Information (ESI) available: Experimental section, SXRD, IR, TG-DTA, PXRD, Natural population analyses, catalytic results, CH_3OH sorption/desorption isotherms. CCDC 2128347 for 1_$\mathbf{BW_{12}}$, 2128348 for 1_$\mathbf{SiW_{11}Nb}$ and 2128349 for 1_$\mathbf{SiW_{11}Ta}$. See DOI: 10.1039/x0xx00000x

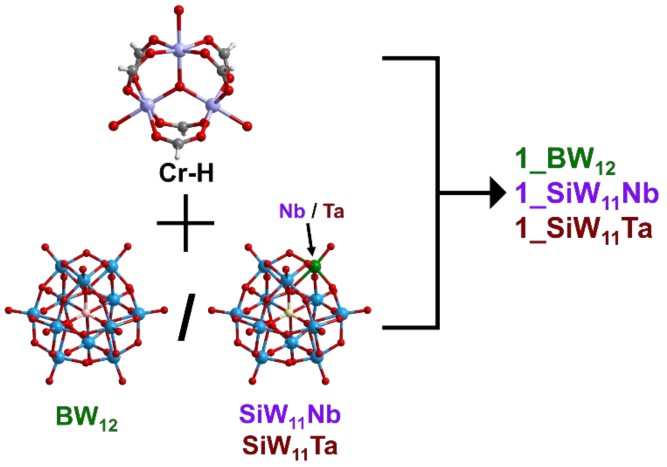

Fig. 1 Molecular structures of $[Cr_3O(OOCH)_6(H_2O)_3]^+$ (**Cr-H**), $[BW_{12}O_{40}]^{5-}$ (**BW$_{12}$**), $[SiW_{11}NbO_{40}]^{5-}$ (**SiW$_{11}$Nb**), $[SiW_{11}TaO_{40}]^{5-}$ (**SiW$_{11}$Ta**), and schematic illustration of the formation of PICs (**1_POMs**).

spectrometry (ICP-OES), X-ray fluorescence (XRF), atomic absorption spectrometry (AAS), CHN combustion analysis, and thermogravimetry (TG, Figs. S4–S6). The results showed that **1_POMs** contained a macrocation and a POM in a 1 : 1 ratio, and four K^+ ions to compensate the surplus negative charge of the POMs. The formulas of the **1_POMs** were determined as $K_4[Cr_3O(OOCH)_6(H_2O)_3][BW_{12}O_{40}]·13H_2O$ (**1_BW$_{12}$**), $K_4[Cr_3O(OOCH)_6(H_2O)_3][SiW_{11}NbO_{40}]·11H_2O$ (**1_SiW$_{11}$Nb**), and $K_4[Cr_3O(OOCH)_6(H_2O)_3][SiW_{11}TaO_{40}]·13H_2O$ (**1_SiW$_{11}$Ta**).

Single crystal X-ray diffraction (SXRD) analysis showed that **1_POMs**[§] and the previously reported PIC composed of $[Cr_3O(OOCH)_6(H_2O)_3]^+$, $[BW_{12}O_{40}]^{5-}$, and Rb^+ ions are isostructural.[27] The crystal structure of **1_BW$_{12}$** will be illustrated as an example (Fig. 2, Figs. S7 and S8 for thermal ellipsoids and Table S1 for the crystallographic data of **1_POMs**). As shown in Fig. 3a, $[BW_{12}O_{40}]^{5-}$ (A) and $[Cr_3O(OOCH)_6(H_2O)_3]^+$ (B) are arrayed along the *c*-axis to form a column with ABAB packing sequence. Two types of K^+ ions (K1 and K2) are bridged by the oxygen atoms of water of crystallization, and each K^+ ion is coordinated by the oxygen atoms of water of crystallization, $[BW_{12}O_{40}]^{5-}$, and $[Cr_3O(OOCH)_6(H_2O)_3]^+$ (Fig. 3b). In detail, K1 is coordinated by eight oxygen atoms: two from formates in $[Cr_3O(OOCH)_6(H_2O)_3]^+$ with K-O distances of 2.83 and 3.20 Å; one from a terminal oxygen in $[BW_{12}O_{40}]^{5-}$ with K-O distance of 2.83 Å; one from a bridging oxygen in $[BW_{12}O_{40}]^{5-}$ with K-O distance of 3.00 Å; two from water in μ_1-coordination with K-O distances of 2.72 and 2.90 Å; two from water in μ_2-coordination with K-O distances of 2.75 and 3.29 Å. K2 is coordinated by ten oxygen atoms: one from a coordination water molecule in $[Cr_3O(OOCH)_6(H_2O)_3]^+$ with K-O distance of 2.86 Å; two from formates in $[Cr_3O(OOCH)_6(H_2O)_3]^+$ with K-O distances of 2.81 and 2.99 Å; three from terminal oxygens in $[BW_{12}O_{40}]^{5-}$ with K-O distances of 2.83 Å and 2.89 Å; one from a bridging oxygen in $[BW_{12}O_{40}]^{5-}$ with K-O distance of 3.25 Å; one from water in μ_1-coordination with K-O distance of 2.99 Å; two from water in μ_2-coordination with K-O distances of 2.88 and 3.33 Å (Fig. 3c). In this way, the columns running parallel to each other are interlinked by the aid of K^+ ions (Fig. 3d). As a result, closed pores with an aperture of 3.6 Å × 3.6 Å and a length of 13.2 Å are formed in the gap between the columns (Fig. 3e). The void analysis by CSD mercury[28] indicates that the void volume in **1_BW$_{12}$** is 7.8% of the unit cell. In the crystal structures of **1_SiW$_{11}$Nb** and **1_SiW$_{11}$Ta**, the positions of the substituted Nb/Ta could not be determined due to disordering. In **1_SiW$_{11}$Nb**, the occupancies of Nb in the twelve $[MO_6]$ were

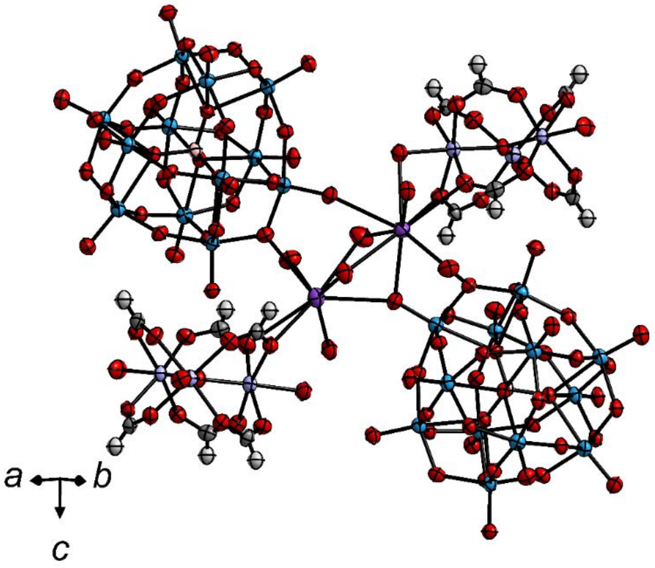

Fig. 2 ORTEP drawing of **1_BW$_{12}$** showing thermal ellipsoids at the 50% probability level. Color codes: W: blue; B: pink; O: red; Cr: violet; K: purple; C: grey; H: light grey.

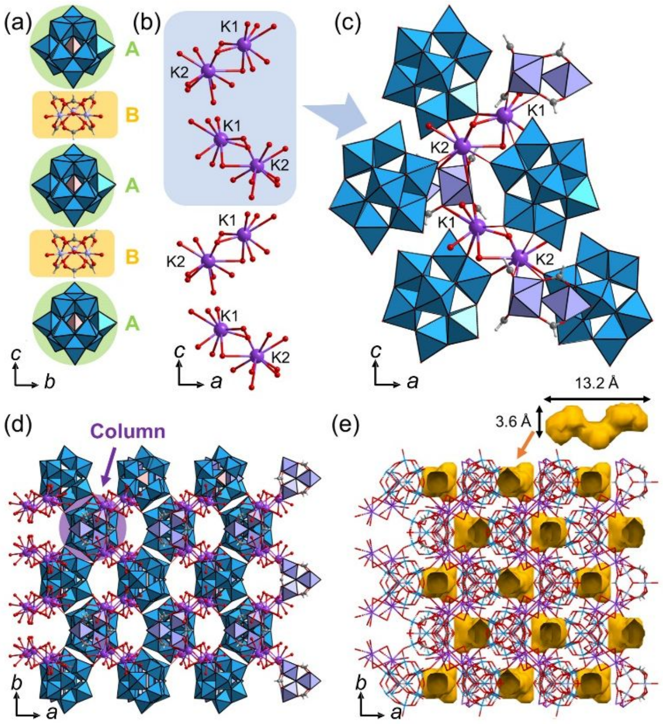

Fig. 3 Crystal structure of **1_BW$_{12}$**. Color codes: W: blue; B: pink; O: red; Cr: violet; K: purple; C: grey; H: light grey; $[WO_6]$: blue octahedra; $[CrO_6]$: violet octahedra; $[BO_4]$: pink tetrahedra. (a) The column composed of $[BW_{12}O_{40}]^{5-}$ (A) and $[Cr_3O(OOCH)_6(H_2O)_3]^+$ (B) along the *c*-axis. (b) The 1D-chain composed of K^+ ions and oxygen atoms. (c) Local views of the coordination environments of K1 and K2. (d) The columns are connected by K^+ ions to form the 3D-structures. (e) Void space (in yellow) is depicted with a probe radius of 1.2 Å.

refined freely and the sum was fixed on 1. In **1_SiW$_{11}$Ta**, the occupancy of Ta in each of the twelve [MO$_6$] was fixed on 1/12. The bulk purities of **1_POMs** were confirmed by the powder X-ray diffraction (PXRD) patterns (Figs. S9–S14); the experimental PXRD patterns were in accordance with those calculated from the crystallographic data.

We decided to carry out Knoevenagel condensation of benzaldehyde with malononitrile as a model base-catalyzed reaction to investigate the effect of Nb/Ta-substitution on basicity (Scheme 1).¶ As the guest sorption properties may play an important role in the base catalysis of **1_POMs**, the sorption isotherms of polar (H_2O, CH_3OH, and CH_3CN at 298 K) and nonpolar (N_2 at 77 K) molecules were measured. As shown in Figs. S18–S20, **1_POMs** exhibited similar sorption properties due to the analogous crystal structures. The uptakes of non-polar N_2 were negligible (< 0.1 mol/mol), probably because N_2 can only adsorb on the surface and cannot diffuse between the closed pores. On the other hand, the uptakes of small polar molecules (H_2O and CH_3OH) exceeded 10 mol/mol at high relative pressures (P/P_0 > 0.85). The desorption branch was measured for CH_3OH, which overlapped with the sorption branch at high relative pressures while a hysteresis existed at low pressures. Such low-pressure hysteresis has been explained by specific host–guest interactions, which alters the crystal structure of the host, and the guest can very slowly escape during the desorption run.[29] In addition, measurable amounts (> 0.5 mol/mol) of CH_3CN, whose molecular size is larger than the aperture of the closed pores, were sorbed. These results show that polar molecules are sorbed in **1_POMs** despite having only closed pores. These phenomena can be explained by the flexible local structures of PICs based on the compensation of lattice enthalpies by host–guest ion–dipole interactions.[29]

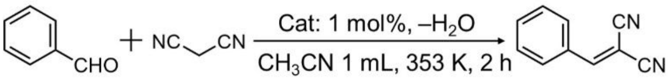

Scheme 1 Knoevenagel condensation of benzaldehyde and malononitrile

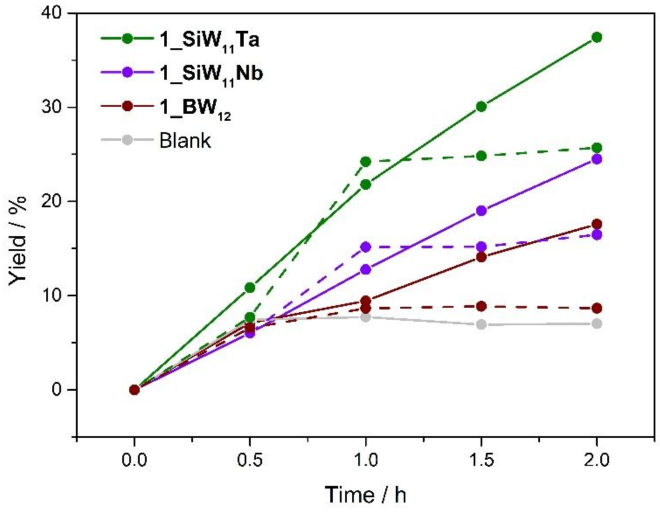

Fig. 4 Time courses of Knoevenagel condensation catalyzed by **1_SiW$_{11}$Ta** (green), **1_SiW$_{11}$Nb** (purple), **1_BW$_{12}$** (brown), and blank test (gray). The broken lines show the leaching tests after the removal of catalysts at 1h.

Table 1 Catalytic results in Knoevenagel condensation reaction[a]

Entry	Catalysts	Conversion / %	Yield[b] / %	Selectivity[c] / %
1	Blank	16	8	50
2	**1_SiW$_{11}$Ta**	50	42	83
3	**1_SiW$_{11}$Nb**	31	25	79
4	**1_BW$_{12}$**	25	19	76

[a]Reaction conditions: 0.01 mmol catalyst, 1.0 mmol benzaldehyde, 1.0 mmol malononitrile, 10 mg biphenyl, 1 mL CH_3CN, 353 K, 2 h. [b]Yield of benzalmalononitrile. [c]Selectivity to benzalmalononitrile.

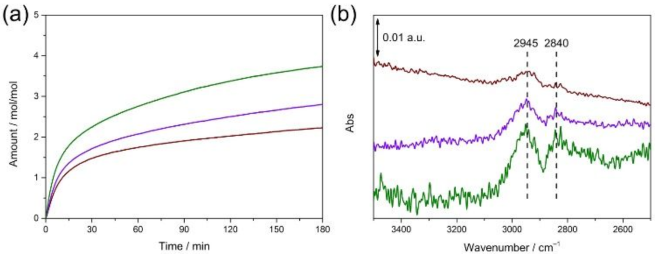

Fig. 5 (a) Time courses of CH_3OH sorption by **1_POMs** at 303 K. (b) Difference *in situ* FT-IR spectra of CH_3OH adsorbed on **1_POMs**. Color code: **1_SiW$_{11}$Ta** (green), **1_SiW$_{11}$Nb** (purple), and **1_BW$_{12}$** (brown).

The catalytic results and time courses of the Knoevenagel condensation are presented in Table 1 and Fig. 4, respectively (see Table S2 for the full results). The product (benzalmalononitrile) yield in the absence of a catalyst was 8% (entry 1). As for **1_POMs**, the product yields and selectivities increased in the order of **1_BW$_{12}$** (19% and 76%, entry 4) < **1_SiW$_{11}$Nb** (25% and 79%, entry 3) < **1_SiW$_{11}$Ta** (42% and 83%, entry 2). While the catalytic performances of the physical mixtures of POM and macrocation (entries 1–3 in Table S2) were similar to those of **1_POMs**, partial dissolution of catalysts into the reaction solution were observed. These results suggest the importance of solidifying the POMs via Coulomb interaction into the nanoscale reaction field. The reactions completely stopped by the removal of **1_POMs** by hot filtration after 1 h, showing that the catalysis is truly heterogeneous (Fig. 4). Moreover, **1_POMs** can be reused at least twice without significant changes in the structures (entries 4–9 in Table S2; Figs. S1–S3 for FT-IR; Figs. S9, S11, and S13 for PXRD). Since **1_POMs** are isostructural, the differences in catalytic activities can be ascribed to the substitution of Nb/Ta with W in the POMs.

Then, we utilized CH_3OH as a probe molecule[30] to characterize the basicity of **1_POMs**. As stated above, the CH_3OH sorption–desorption isotherms of isostructural **1_POMs**

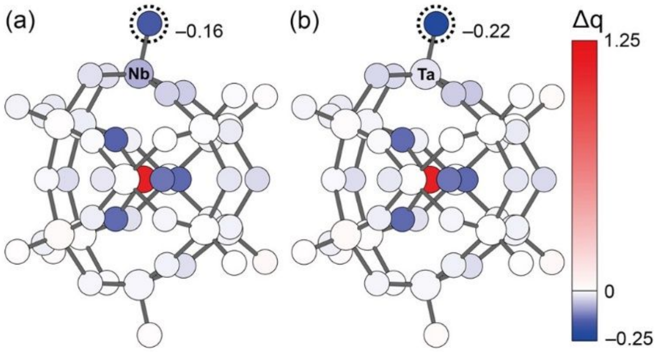

Fig. 6 Difference of natural charges between (a) **SiW$_{11}$Nb** or (b) **SiW$_{11}$Ta** and **BW$_{12}$**

were similar to each other (Figs. S18–S20); this result suggests that the amounts of CH_3OH uptake and thus the thermodynamics of CH_3OH sorption depend on the crystal structure.[31] Fig. 5a shows the time courses of CH_3OH sorption by **1_POMs**, reflecting the kinetics of CH_3OH sorption. The rates of CH_3OH sorption increased in the order of **1_BW$_{12}$** < **1_SiW$_{11}$Nb** < **1_SiW$_{11}$Ta**, which follows the order of basicity. Furthermore, the states of CH_3OH sorbed on **1_POMs** were investigated by *in situ* FT-IR spectroscopy (Fig. 5b);[20,32] **1_POMs** were exposed to a CH_3OH vapor of ca. 10 kPa at room temperature then evacuated to attain > 0.05 kPa to remove gaseous and weakly sorbed CH_3OH. We did not wait for pressure equilibrium to be attained so that this measurement is supposed to reflect the kinetics of CH_3OH desorption. As shown in Fig. 5b, the difference spectra of CH_3OH sorbed on **1_POMs** showed bands at 2945 cm^{-1} and 2840 cm^{-1}, which can be assigned to the asymmetric and symmetric CH_3 stretching vibration modes, respectively, of molecularly sorbed CH_3OH. Notably, the intensity of the bands increased in the order of **1_BW$_{12}$** < **1_SiW$_{11}$Nb** < **1_SiW$_{11}$Ta**, suggesting that the amounts of strongly interacting CH_3OH molecules increase in the same order. All these results demonstrate that the basicity increases in the order of **1_BW$_{12}$** < **1_SiW$_{11}$Nb** < **1_SiW$_{11}$Ta**, which is reflected in the kinetics of CH_3OH sorption–desorption behaviors.

To attain a better understanding of the basicity of **1_POMs**, theoretical calculations were performed by the density functional theory (DFT) method.[33] The results of natural population analyses of the POMs are summarized in Tables S3–S5. To investigate the effect of Nb/Ta-substitution on the electron density distribution within the POMs, we compared the natural charges of atoms at equivalent positions in Nb/Ta-substituted POMs (**SiW$_{11}$Nb** and **SiW$_{11}$Ta**) and non-substituted POM (**BW$_{12}$**). The differences are depicted in Fig. 6; the natural charges of terminal oxygen of the substituted Nb/Ta atom in **SiW$_{11}$Nb** and **SiW$_{11}$Ta** increased negatively by 0.16 and 0.22, respectively. This trend is in line with the order of basicity and catalytic activities of the PICs (**1_BW$_{12}$** < **1_SiW$_{11}$Nb** < **1_SiW$_{11}$Ta**), and in inverse relationship to the electronegativity of the metals (Ta < Nb < W).[23] There were no significant differences in natural charges of other terminal or bridging oxygen atoms. These results indicate that the increase in basicity of **1_POMs** could be ascribed to the increase in electron density of terminal oxygen of the substituted Nb/Ta atom.

In summary, isostructural PICs (**1_POMs**) composed of a non-substituted POM ($[BW_{12}O_{40}]^{5-}$: **BW$_{12}$**) or Nb/Ta mono-substituted POMs ($[SiW_{11}NbO_{40}]^{5-}$: **SiW$_{11}$Nb** and $[SiW_{11}TaO_{40}]^{5-}$: **SiW$_{11}$Ta**) were synthesized and characterized. The catalytic activities in base-catalyzed Knoevenagel condensation reaction with **1_POMs** as solid catalysts increased in the order of **1_BW$_{12}$** < **1_SiW$_{11}$Nb** < **1_SiW$_{11}$Nb**. The Nb/Ta-substitution effects on basicity were demonstrated experimentally by the sorption–desorption isotherms, time courses of sorption, and *in situ* IR spectroscopy with CH_3OH as a probe molecule; the order of basicity was reflected in the kinetics of CH_3OH sorption-desorption behaviors. Theoretical calculations indicated that the negative charges of terminal oxygen increase in the order of W < Nb < Ta in the POMs, which is in line with the basicity and catalytic activities of the **1_POMs**. While it is often explained that the increase in negative charge (or charge density) of the POM molecule increases its basicity, since the three different Keggin-type POMs as components of **1_POMs** possess equal negative charge (–5), we can conclude that the basicity is also affected by the character of the substituted element itself. These findings demonstrate that PICs based on POMs can serve as a tailorable platform for the rational design of solid base catalysts by fine-tuning the compositions.

Author Contributions

Z.W. performed the syntheses and characterization of the compounds with help from N.O.; D.Y. carried out the DFT calculations; T.K. helped the XRF measurements; Y.K. helped the *in situ* IR measurements; Z.W., N.O., and S.U. wrote the manuscript; S.U. conceived and designed the project. All authors discussed the results and commented on the manuscript.

Conflicts of interest

There are no conflicts to declare.

Acknowledgements

This work was supported by the JSPS Grants-in-Aid for Scientific Research from MEXT of Japan (JP20H02750, JP21K14639, and JP21K18975), the International Network on Polyoxometalate Science at Hiroshima University, and JSPS Core-to-Core program. Z.W. wishes to acknowledge support from the JST SPRING, Grant Number JPMJSP2108.

Notes and references

‡Synthesis of $K_4[Cr_3O(OOCH)_6(H_2O)_3][BW_{12}O_{40}]\cdot 13H_2O$ (**1_BW$_{12}$**): $[Cr_3O(OOCH)_6(H_2O)_3](OOCH)\cdot nH_2O$ (0.1 g, 0.167 mmol) was dissolved in 10 mL of aqueous HNO_3 solution (0.01 M, pH = 2). $K_5[BW_{12}O_{40}]\cdot nH_2O$ (0.3 g, 0.09 mmol) and KCl (0.2 g, 2.68 mmol) were added to the solution followed by stirring for 2 min. The solution was kept at 277 K for one week and green needle crystals were obtained. Elemental analysis (%): Calcd: C 1.92, B 0.29, K 4.18, Cr 4.15, W 58.93. Found: C 2.00, B 0.33, K 4.01, Cr 4.18, W 56.21. FT-IR (KBr pellet, cm^{-1}, Fig. S1): $\nu_{asym}(OCO)$ 1630, $\nu_{sym}(OCO)$ 1374, $\nu_{asym}(B–O_a)$ 1006, $\nu_{asym}(W–O_a)$ 964, $\nu_{asym}(W–O_b–W)$ 908, $\nu_{asym}(W–O_c–W)$ 812.

Synthesis of $K_4[Cr_3O(OOCH)_6(H_2O)_3][SiW_{11}NbO_{40}]\cdot 11H_2O$ (**1_SiW$_{11}$Nb**): $[Cr_3O(OOCH)_6(H_2O)_3]OOCH\cdot nH_2O$ (0.1 g, 0.167 mmol) was dissolved in 10 mL of aqueous HCl solution (0.01 M, pH = 2). $K_5[SiW_{11}Nb(O_2)O_{39}]$ (0.3 g, 0.09 mmol) and KCl (0.2 g, 2.68 mmol) were added to the solution followed by stirring for 2 min. The solution was kept at 277 K for 2 days and green block crystals were obtained. Elemental analysis (%): Calcd: C 2.03, Si 0.79, K 4.42, Cr 4.41, W 57.11. Found: C 2.16, Si 1.11, K 4.04, Cr 4.45, W 56.38. The molar ratio of Nb : W according to XRF was 1 : 10.1, and fairly agreed with the calculation (1 : 11). FT-IR (KBr pellet, cm^{-1}, Fig. S2): $\nu_{asym}(OCO)$ 1634, $\nu_{sym}(OCO)$ 1376, $\nu_{asym}(Si–O_a)$ 1012, $\nu_{asym}(W–O_a)$ 974, $\nu_{asym}(W–O_b–W)$ 914, $\nu_{asym}(W–O_c–W)$ 790.

Synthesis of $K_4[Cr_3O(OOCH)_6(H_2O)_3][SiW_{11}TaO_{40}]\cdot 13H_2O$ (**1_SiW$_{11}$Ta**): $[Cr_3O(OOCH)_6(H_2O)_3]OOCH\cdot nH_2O$ (0.1 g, 0.167 mmol) was dissolved in 10 mL of aqueous HCl solution (0.01 M, pH = 2). $K_5[SiW_{11}Ta(O_2)O_{39}]\cdot 18H_2O$ (0.3 g, 0.09 mmol) and KCl (0.2 g, 2.68 mmol) were added to the solution followed by stirring for 2 min. The solution was kept at 277 K for one week and green block crystals were obtained. Elemental analysis (%): Calcd: C 2.03, Si 0.79, K 4.41, Cr 4.40, W 56,14. Found: C 2.02, Si 1.16, K 4.05, Cr 4.21, W 55.84. The molar ratio of Ta : W according to XRF was 1 : 10.2, and fairly agreed with the calculation (1 : 11). FT-IR (KBr pellet, cm^{-1}, Fig. S3): ν_{asym}(OCO) 1633, ν_{sym}(OCO) 1382, ν_{asym}(Si–O_a) 1015, ν_{asym}(W–O_a) 974, ν_{asym}(W–O_b–W) 918, ν_{asym}(W–O_c–W) 786.

§Single crystal X-ray diffraction data of **1_BW$_{12}$**, **1_SiW$_{11}$Nb**, and **1_SiW$_{11}$Ta** were collected at 153 K with a HyPix-6000 area detector by using a Rigaku Saturn diffractometer with graphite monochromated Mo Kα radiation (λ = 0.71073 Å). The data reduction and correction were processed with CrysAlisPro software. Muti-scan and sphere type absorption corrections were performed. Due to the insufficient quality of the crystal and diffraction data, we failed to apply crystal face-indexing numerical type absorption corrections. All the structures are solved by intrinsic phase method (SHELXT[34]) and refined by the full-matrix least-squares method on F^2 using SHELXL-2019/2 crystallographic software package[35] through Olex2[36]. All the atoms were refined anisotropically, and the position of hydrogen atoms on the formic acid are theoretically calculated and refined isotropically. The Platon/Squeeze[37] program was used to mask the electron density of the disordered water molecules and in the voids. The program suggested that 90.5 (**1_BW$_{12}$**), 85.5 (**1_SiW$_{11}$Nb**) and 82.5 (**1_SiW$_{11}$Ta**) electrons exist in the solvent-accessible volume per formula, which were roughly consistent with the amounts of unassigned water of crystallization in the voids. Crystal data for **1_BW$_{12}$**: orthorhombic *Pnma* (#62), a = 24.3679(4), b = 15.9691(2), c = 16.9507(2), V = 6596.11(16), Z = 4, R_{int} = 0.0495, R_1 = 0.0637, wR_2 = 0.1684, GOF = 1.175, max. / min. residual electron density: 5.97 / –2.67. Crystal data for **1_SiW$_{11}$Nb**: orthorhombic *Pnma* (#62), a = 24.4216(4), b = 16.0494(2), c = 17.0259(2), V = 6673.31(17), Z = 4, R_{int} = 0.0530, R_1 = 0.0658, wR_2 = 0.1732, GOF = 1.055, max. / min. residual electron density: 4.42 / –1.96. Crystal data for **1_SiW$_{11}$Ta**: orthorhombic *Pnma* (#62), a = 24.4565(4), b = 16.0527(4), c = 17.0555(4), V = 6695.9(3), Z = 4, R_{int} = 0.1400, R_1 = 0.1052, wR_2 = 0.2644, GOF = 1.069, max./min. residual electron density: 9.38/–3.22. Relatively large residual electron densities generally correspond to Fourier series truncation ripples near heavy atoms, which cause an imperfect fitting of the structure model in high electron density areas and are characteristic to polyoxotungstates. Table S1 summarizes the crystallographic data.

¶Knoevenagel condensation reaction was carried out in a glass tube equipped with a magnetic stirrer. In a typical run of reaction, a mixture of benzaldehyde (106 mg, 1.0 mmol), malononitrile (66 mg, 1.0 mmol), biphenyl (10 mg, internal standard), and catalyst (0.01 mmol) in CH_3CN (1 mL) was stirred at 353 K. The amounts of products (benzalmalononitrile) were followed by gas chromatography using a GC-2014 (Shimadzu) fitted with a HP-5 column (60 m × 0.32 mm × 0.25 µm) and a flame ionization detector (FID). The reaction solution (with the solid catalyst) was sampled periodically and injected directly into the GC system. Since the particle size of solid catalysts may affect the catalysis, we checked that the results were essentially the same with thoroughly ground powder or microcrystalline compounds. The results of Knoevenagel condensation reaction over various solid catalysts and conditions were summarized in our recent work (Table S5 of ref.26). In the present work, catalytic reaction was utilized as a characterization of the compounds, and we note that there are superior catalysts for this reaction. We also performed this reaction at room temperature in ethanol, and the trend in catalytic activities were unchanged (Fig. S21).

1 H. Pines and W. M. Stalick, *Base-catalyzed reactions of hydrocarbons and related compounds*, Academinc Press, 1977.

2 S. E. Denmark and R. A. Stavenger, *Acc. Chem. Res.*, 2000, **33**, 432–440.

3 J. Seayad, A. Tillack, C. G. Hartung and M. Beller, *Adv. Synth. Catal.*, 2002, **344**, 795–813.

4 K. Tanabe and W. F. Hölderich, *Appl. Catal., A*, 1999, **181**, 399–434.

5 A. Diallo, Y. Zhao, H. Wang, S. Li, C. Ren and Q. Liu, *Org. Lett.*, 2012, **14**, 5776–5779.

6 M. Zhang and J. Zhang, *Chem. Eur. J.*, 2014, **20**, 399–404.

7 J. J. Newton, R. Britton and C. M. Friesen, *J. Org. Chem.*, 2018, **83**, 12784–12792.

8 Y. Ono, *J. Catal.*, 2003, **216**, 406–415.

9 Y. Ono and H. Hattori, *Solid base catalysis*, Springer-Verlag Berlin Heidelberg, 2011.

10 H. Hattori, *Appl. Catal., A*, 2015, **504**, 103–109.

11 P. Gupta and S. Paul, *Catal. Today*, 2014, **236**, 153–170.

12 W. Gong, Y. Liu, H. Li and Y. Cui, *Coord. Chem. Rev.*, 2020, **420**, 213400.

13 P. Sudarsanam, N. K. Gupta, B. Mallesham, N. Singh, P. N. Kalbande, B. M. Reddy and B. F. Sels, *ACS Catal.*, 2021, **11**, 13603–13648.

14 Y. Shimoyama, Z. Weng, N. Ogiwara, T. Kitao, Y. Kikukawa and S. Uchida, *Dalton Trans.*, 2020, **49**, 10328–10333.

15 M. T. Pope and A. Müller, *Angew. Chem., Int. Ed. Engl.*, 1991, **30**, 34–48.

16 C. L. Hill, *Chem. Rev.*, 1998, **98**, 1–2.

17 L. Cronin and A. Müller, *Chem. Soc. Rev.*, 2012, **41**, 7333–7334.

18 Y. Shimoyama and S. Uchida, *Chem. Lett.*, 2021, **50**, 21–30.

19 K. Kamata and K. Sugahara, *Catalysts*, 2017, **7**, 1–24.

20 X. López, C. Bo and J. M. Poblet, *J. Am. Chem. Soc.*, 2002, **124**, 12574–12582.

21 W. Ge, X. Wang, L. Zhang, L. Du, Y. Zhou and J. Wang, *Catal. Sci. Technol.*, 2016, **6**, 460–467.

22 S. Hayashi, S. Yamazoe, K. Koyasu and T. Tsukuda, *RSC Adv.*, 2016, **6**, 16239–16242.

23 S. Hayashi, N. Sasaki, S. Yamazoe and T. Tsukuda, *J. Phys. Chem. C*, 2018, **122**, 29398–29404.

24 Q. Xu, Y. Niu, G. Wang, Y. Li, Y. Zhao, V. Singh, J. Niu and J. Wang, *Mol. Catal.*, 2018, **453**, 93–99.

25 S. Hayashi, S. Yamazoe and T. Tsukuda, *J. Phys. Chem. C*, 2020, **124**, 10975–10980.

26 Z. Weng, N. Ogiwara, T. Kitao, Y. Kikukawa, Y. Gao, L. Yan and S. Uchida, *Nanoscale*, 2021, **13**, 18451–18457.

27 S. Uchida, R. Kawamoto and N. Mizuno, *Inorg. Chem.*, 2006, **45**, 5136–5144.

28 C. F. Macrae, I. Sovago, S. J. Cottrell, P. T. A. Galek, P. McCabe, E. Pidcock, M. Platings, G. P. Shields, J. S. Stevens, M. Towler and P. A. Wood, *J. Appl. Crystallogr.*, 2020, **53**, 226–235.

29 S. Uchida and N. Mizuno, *Chem. Eur. J.*, 2003, **9**, 5850–5857.

30 H. Petitjean, K. Tarasov, F. Delbecq, P. Sautet, J. M. Krafft, P. Bazin, M. C. Paganini, E. Giamello, M. Che, H. Lauron-Pernot and G. Costentin, *J. Phys. Chem. C*, 2010, **114**, 3008–3016.

31 S. Uchida and N. Mizuno, *Coord. Chem. Rev.*, 2007, **251**, 2537–2546.

32 S. Kanai, I. Nagahara, Y. Kita, K. Kamata and M. Hara, *Chem. Sci.*, 2017, **8**, 3146–3153.

33 C. Wu, L. Yan, T. Zhang and Z. Su, *Inorg. Chem. Front.*, 2015, **2**, 246−253.

34 G. M. Sheldrick, *Acta Crystallogr., Sect. A: Found. Adv.*, 2015, **71**, 3–8.

35 G. M. Sheldrick, *Acta Crystallogr., Sect. C: Struct. Chem.*, 2015, **71**, 3–8.

36 O. V. Dolomanov, L. J. Bourhis, R. J. Gildea, J. A. K. Howard and H. Puschmann, *J. Appl. Crystallogr.*, 2009, **42**, 339–341.

37 A. L. Spek, *Acta Crystallogr., Sect. C: Struct. Chem.*, 2015, **71**, 9–18.